DATA ANALYTICS AND APPLIED MATHEMATICS
E-ISSN: 2773-4854
VOLUME 7, ISSUE 1, 2026, 39 - 49
DOI: https://doi.org/10.15282/daam.v7i1.13685

RESEARCH ARTICLE

The numerical solutions in three-dimensional double diffusive Jeffrey fluid flow with injection effect

Nanthini Balakrishnan[1], Fatin Nur Asyikyn Pazil[1], Shahanaz Parvin[2], Nurul Syuhada Ismail[3], Siti Suzilliana Putri Mohamed Isa[1,4]*

[1]Institute for Mathematical Research (INSPEM), Universiti Putra Malaysia, 43400 Serdang, Selangor, Malaysia
[2]Government Barhamganj College, Shibchar, Madaripur, Bangladesh
[3]Centre for Pre-University Studies, Universiti Malaysia Sarawak, 93400 Kota Samarahan, Sarawak, Malaysia
[4]Centre for Foundation Studies in Science of Universiti Putra Malaysia, Universiti Putra Malaysia, 43400 Serdang, Selangor, Malaysia

Abstract - Various engineering and industrial applications are employing the idea of convective double diffusive fluid stream, particularly through an extending surface. In recent times, many researchers have been interested in investigating the stream of Jeffrey fluid due to its application in modelling the behaviour of polymer melts during processing, such as extrusion or injection moulding. Therefore, this study is intended to develop a mathematical model for double diffusive Jeffrey fluid streaming past an elongating sheet. The influence of the injection parameter, together with the non-Newtonian properties, is taken into consideration. By using a similarity transformation, the governing equations, boundary conditions, and physical parameters have been altered into ordinary differential equations. As a result, it is found that the fluid flow is influenced by the injection rate, mixed convection, and buoyancy ratio. This statement is supported by the study, which shows the uplift of velocity as the injection rate parameter increases for larger values of boundary layer thickness. The stream velocity also surges with the rise of the mixed convection parameter and the buoyancy parameter, resulting in a slimmer boundary layer. Meanwhile, the thermal and mass exchange properties depend on the Soret–Dufour factor, where the temperature profile augments for several values of Dufour parameter, and the concentration profile increases for diverse values of Soret parameter.

Article history
Received : 23 December 2025
Revised : 20 February 2026
Accepted : 7 March 2026
Published : 31 March 2026

Keywords
Heat-mass transfer
Double diffusive
Jeffrey fluid flow
Injection effect

1. Introduction

Jeffrey fluid is an example of the non-Newtonian fluid that portrays viscosity property (liquid characteristic) and elasticity feature (solid behavior). The examples of Jeffrey fluid are blood, polymer, honey, paint, etc. This type of fluid has been implemented in blood flow modelling [1], polymer production [2], and industrial processes involving suspensions and emulsions [3-4]. Meanwhile, double diffusive convection in the fluid flow system occurs when two diffusion processes of heat and mass components are competing. The examples of double diffusive process are the saltwater in the ocean, volcanic activity due to the mantle and magma chambers, nuclear reactors, and so on. The studies of double diffusive convection of Jeffrey fluid flow bounded between rotating cone and disk [5], vertical channel [6], asymmetric ciliated channel [7], and inclined surface [8] have been reported. Besides, double-diffusive convection in fluids other than the Jeffrey model has been described; for example, in Casson fluids [9–11], Maxwell fluids [12-13], Carreau fluids [14-15], and nanofluids [16-17]. On the other hand, Soret and Dufour impacts are the two incorporated exchange processes that arise in heat-mass transfer. The Soret effect can be described as the mass transport from a greater temperature to a region with lower temperature within a fluid. Mass diffusion, or Dufour effect occurs when the thermal energy is transferred due to the concentration gradient [18]. The behavior of fluid stream when it interacts with a magnetic flux is known as magnetohydrodynamics (MHD), and the fluid types are plasmas, liquid water, and salt water. The applications of MHD are proven in MHD generators and pumps. The flow of conducting fluid owns kinetic energy which can be turned into electrical energy. Otherwise, MHD pumps are used in cooling systems in nuclear reactors. The research of MHD Jeffrey fluid stream with the Soret-Dufour influences has been issued for various boundaries, such as the inclined channel [19-20], horizontal channel [21], and flat sheet [22-23]. The MHD and Soret-Dufour effects on other non-Newtonian fluids are described by Fard et al. [24], Sudarmozhi et al. [25], and Prajapati and Meher [18].

The viscous 3D magnetohydrodynamics stream of Newtonian fluid passing by a plate elongating exponentially was analyzed by Parvin et al. [26] to study the flow, thermal, and mass movement. In contrast, the current study focuses on the thermal properties of a three-dimensional Jeffrey fluid in an expanding plane with the injection effect, building upon the foundational work on Jeffrey fluids over stretching sheets reported by Ahmad et al. [23]. The expanding plane is chosen as a flow model to account for flows in geometries where the plane area increases with flow direction. It also presents geometric inhomogeneity that more truly reflects practical complex industrial flow fields and biological flow domains. Furthermore, the presence of the injection effect permits a more realistic modelling of practical systems such as filtration apparatus, biomedical applications (drug delivery), cooling systems, and chemical reactors. Injection also plays a key role in controlling flow separation and enhancing mixing efficiency. This paper also formulates the mathematical formulation and analyzed the parameters such as mixed convection parameter, buoyancy ratio, injection rate, Soret number and Dufour number to solve the non-Newtonian fluid by MATLAB bvp4c coding. The variations of Jeffrey fluid

***CORRESPONDING AUTHOR | Siti Suzilliana Putri Mohamed Isa**| ✉ ctsuzilliana@upm.edu.my

flow components, thermal components and mass components for different parameters are probed and given detailed explanation.

2. Methodology

An incompressible, steady, two-dimensional Jeffrey fluid is considered to stream through 3D horizontal extending plane ($x-$ and $y-$axes). The 3D model of double diffusive Jeffrey fluid stream in Figure 1 has shown the physical layout with a coordinate structure. The components of the fluid's velocity in the horizontal and vertical directions are indicated by $p_w(x,y) = \mu_1 P_0 e^{(x+y)/L}$ and $q_w(x,y) = \mu_2 Q_0 e^{(x+y)/L}$, respectively. The constant $Q_0 > 0$ is assumed as $P_0 = Q_0$ in the velocity's components, p_w and q_w. The variable temperature of the surface and the fluid concentration are represented as $T_w(x,y) = T_\infty + T_0 e^{(x+y)/2L}$ and $C_w(x,y) = C_\infty + C_0 e^{(x+y)/2L}$. The constant peripheral temperature T_∞ and concentration C_∞ are regarded.

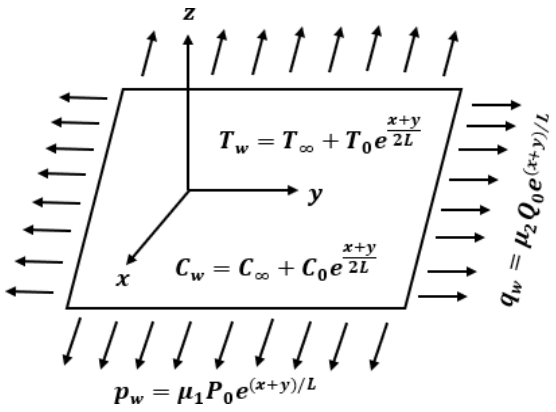

Figure 1. The layout of 3D double diffusive Jeffrey fluid stream model

The ruling equations for the boundary layer can be stated as [23]:

$$\frac{\partial P}{\partial x} + \frac{\partial q}{\partial y} + \frac{\partial r}{\partial z} = 0 \tag{1}$$

$$p\frac{\partial p}{\partial x} + q\frac{\partial p}{\partial y} + r\frac{\partial p}{\partial z} = \frac{\nu}{1+\mu_1}\left[\frac{\partial^2 p}{\partial y^2} + \mu_2\left(p\frac{\partial^3 p}{\partial x \partial y^2} + \frac{\partial p}{\partial y}\frac{\partial^2 p}{\partial x \partial y} - \frac{\partial p}{\partial x}\frac{\partial^2 p}{\partial y^2} + q\frac{\partial^3 p}{\partial y^3}\right)\right] + g\beta_T(T - T_\infty) + g\beta_C(C - C_\infty) - \sigma\frac{\beta_0^2}{\rho}p, \tag{2}$$

$$p\frac{\partial q}{\partial x} + q\frac{\partial q}{\partial y} + r\frac{\partial q}{\partial z} = \frac{\nu}{1+\mu_1}\left[\frac{\partial^2 p}{\partial y^2} + \mu_2\left(p\frac{\partial^3 p}{\partial x \partial y^2} + \frac{\partial p}{\partial y}\frac{\partial^2 p}{\partial x \partial y} - \frac{\partial p}{\partial x}\frac{\partial^2 p}{\partial y^2} + q\frac{\partial^3 p}{\partial y^3}\right)\right] + g\beta_T(T - T_\infty) + g\beta_C(C - C_\infty) - \sigma\frac{\beta_0^2}{\rho}p, \tag{3}$$

$$p\frac{\partial T}{\partial x} + q\frac{\partial T}{\partial y} + r\frac{\partial T}{\partial z} = \alpha\frac{\partial^2 T}{\partial z^2} + \frac{DK}{C_s C_p}\frac{\partial^2 C}{\partial z^2}, \tag{4}$$

$$p\frac{\partial C}{\partial x} + q\frac{\partial T}{\partial y} + r\frac{\partial T}{\partial z} = D\frac{\partial^2 C}{\partial z^2} + \frac{DK}{T_m}\frac{\partial^2 T}{\partial z^2}, \tag{5}$$

where p, q and r are the $x-, y-$ and $z-$ elements of the velocity respectively, the proportion of the relaxation time to the retardation time is indicated by μ_1, where μ_2 is the relaxation time. The kinematic viscosity, which results from the dynamic viscosity μ divided by the fluid's density ρ, is denoted by ν, g is the gravitational acceleration, σ represents conductivity of electricity, α is the heat dispersal, thermal growth's coefficient is β_T, the solutal growth's coefficient is β_C, β_0 is the uniform intensity of magnetic flux, K is the ratio of heat dispersal, T is the fluid's temperature, D is the dispersal of mass, C_s is the susceptibility of the fluid's concentration, C_p denotes the specific heat at constant pressure and T_m is the fluid's mean temperature. The present stream inspection possesses the subsequent boundary constraints [26]:

$$\begin{aligned} &p = p_w(x,y) = \mu_1 P_0 e^{(x+y)/L}, q = q_w(x,y) = \mu_2 Q_0 e^{(x+y)/L} \text{ at } z = 0, \\ &r = R(x,y), T_w(x,y) = T_\infty + T_0 e^{(x+y)/2L}, C_w(x,y) = C_\infty + C_0 e^{(x+y)/2L} \text{ at } y = 0, \\ &p \to 0, q \to 0, T \to T_\infty, C \to C_\infty \text{ as } z \to \infty, \end{aligned} \tag{6}$$

The new similarity conversions are introduced as follows [26]:

$$\eta = \sqrt{\frac{P_0}{2Lv}} e^{\frac{(x+y)}{2L}} z, p = P_0 e^{\frac{(x+y)}{2L}} f'(\eta), q = Q_0 e^{\frac{(x+y)}{2L}} h'(\eta),$$

$$r = -\sqrt{\frac{vP_0}{2L}} e^{\frac{(x+y)}{2L}} [f(\eta) + \eta f'(\eta) + h(\eta) + \eta h'(\eta)], \tag{7}$$

$$T = T_w(x,y) = T_\infty + T_0 e^{\frac{(x+y)}{2L}} \theta(\eta), C = C_w(x,y) = C_\infty + C_0 e^{\frac{(x+y)}{2L}} \phi(\eta)$$

where η depicts the boundary layer thickness, $f'(\eta)$ and $h'(\eta)$ are the velocity profiles along horizontal and vertical axes respectively, $\theta(\eta)$ is the temperature profile and $\phi(\eta)$ is the concentration profile. Utilizing Eq. (7), Eq. (1) has been satisfied. Similarly, Eqs. (2) - (5) have been transformed as below:

$$\begin{aligned} &2[f'(\eta)]^2 + 2h'(\eta)f'(\eta) - f(\eta)f''(\eta) - h(\eta)f''(\eta) = \frac{1}{\eta^2} f'(\eta) + \frac{1}{\eta^2} \eta f''(\eta) + f'''(\eta) \\ &+ \frac{3}{4}\beta^* f'''(\eta)[f'(\eta) + h'(\eta)] + \frac{\beta^* \eta}{8} f^{(iv)}(\eta)[f'(\eta) + h'(\eta)] + \frac{\beta^*}{\eta^2} f'(\eta)[f'(\eta) + h'(\eta)] \\ &+ \frac{3\beta^*}{2\eta} f''(\eta)[f'(\eta) + h'(\eta)] + (1+\mu_1) Ri[\theta(\eta) + N\phi(\eta)] - (1+\mu_1)\frac{M}{\eta^2} f'(\eta), \end{aligned} \tag{8}$$

$$\begin{aligned} &2f'(\eta)h'(\eta) + 2\left[h'^{(\eta)}\right]^2 - h''(\eta)f(\eta) - h''(\eta)h(\eta) = \frac{1}{\eta^2} f'(\eta) + \frac{1}{\eta^2} \eta f''(\eta) + f'''(\eta) \\ &+ \frac{3}{4}\beta^* f'''(\eta)[f'(\eta) + h'(\eta)] + \frac{\beta^* \eta}{8} f^{(iv)}(\eta)[f'(\eta) + h'(\eta)] + \frac{\beta^*}{\eta^2} f'(\eta)[f'(\eta) + h'(\eta)] \\ &+ \frac{3\beta^*}{2\eta} f''(\eta)[f'(\eta) + h'(\eta)] + (1+\mu_1) Ri[\theta(\eta) + N\phi(\eta)] - (1+\mu_1)\frac{M}{\eta^2} f'(\eta), \end{aligned} \tag{9}$$

$$\frac{1}{Pr}\theta''(\eta) - \theta[f'(\eta) + h'(\eta)] + \theta'[f(\eta) + h(\eta)] + Db\phi''(\eta) = 0, \tag{10}$$

$$\frac{1}{Sc}\phi''(\eta) - \phi[f'(\eta) + h'(\eta)] + \phi'[f(\eta) + h(\eta)] + Sr\theta''(\eta) = 0, \tag{11}$$

where β^* is the ratio of Deborah number and energy defined as $\beta = \frac{v\mu_2}{L^2}$ and $E = \frac{v}{P_0 L} e^{-\left(\frac{x+y}{L}\right)}$ respectively, $Pr = \frac{v}{\alpha}$ is the Prandtl number, $Ri = \frac{L^2}{U_0 v} g\beta_T T_0 e^{-\frac{(x+y)}{2L}}$ is the constant mixed convection parameter, $N = \frac{\beta_0 C_0}{\beta_T T_0}$ is the buoyancy ratio, $M = \frac{L^2 \sigma \beta_0^2}{v\rho}$ is the magnetic field, $Sc = \frac{v}{D}$ is the Schmidt number, $Sr = \frac{DKT_0}{T_m C_0 v}$ is the Soret number and $Db = \frac{DK}{C_s C_p}\frac{C_0}{T_0 v}$ is the Dufour number. The boundary conditions as shown in Eq. (6) have been transformed as below:

$$\begin{aligned} &f(0) = I, f'(0) = \mu_1, h(0) = 0, h'(0) = \mu_2, \theta(0) = 1, \phi(0) = 1 \text{ at } \eta = 0, \\ &f'(\eta) \to 0, h'(\eta) \to 0, \theta(\eta) \to 0, \phi(\eta) \to 0 \text{ as } \eta \to \infty, \end{aligned} \tag{12}$$

where $I = -\frac{R(x,y)}{\sqrt{\frac{vP_0}{2L}} e^{\frac{(x+y)}{2L}}}$ is the injection parameter. The skin friction coefficients, C_{fx}, C_{fy} besides local Nusselt number, Nu_x and local Sherwood number, Sh_x are interpreted as following:

$$\begin{aligned} &C_{fx} = \frac{\tau_{xz}}{\rho P_0^2}, C_{fy} = \frac{\tau_{yz}}{\rho Q_0^2}, \\ &Nu_x = \frac{Lq_w}{k(T_w - T_\infty)}, Sh_x = \frac{L}{(C_w - C_\infty)}\left(-\frac{\partial C}{\partial z}\right), \end{aligned} \tag{13}$$

where $\tau_{xz} = \mu\left(\frac{\partial p}{\partial x} + \frac{\partial r}{\partial z}\right)_{z=0}$ and $\tau_{yz} = \mu\left(\frac{\partial q}{\partial x} + \frac{\partial q}{\partial z}\right)_{z=0}$ are the shear stresses along xz and yz planes and $q_w = -k\left(\frac{\partial T}{\partial z}\right)_{z=0}$ is the heat flux on the surface. Substituting Eq. (7) into Eq. (13), the dimensionless form of physical parameters is acquired as shown in Eq. (14).

$$\sqrt{Re_x}e^{-\frac{2(x+y)}{L}}C_{fx}+\frac{1}{2Re_x}=f''(0),\sqrt{Re_y}e^{-\frac{2(x+y)}{L}}C_{fy}+\frac{1}{2Re_y}=h''(0),$$
$$Nu_x\sqrt{\frac{2}{Re_x}}=-\theta'(0),Sh_x\sqrt{\frac{2}{Re_x}}=-\phi'(0), \tag{14}$$

where $Re_x=\frac{LP_0}{\nu}e^{\frac{(x+y)}{L}}$ and $Re_x=\frac{LQ_0}{\nu}e^{\frac{(x+y)}{L}}$ are Reynold's number along x and y axes.

2.1 Numerical Solution

The nonlinear ordinary differential equations are resolved by a bvp4c built-in function in MATLAB. The numerical data of the skin friction coefficient number, the local Nusselt number, local Sherwood number together with the velocity profile along $x-$axis $[f'(\eta)]$ and along $y-$axis $[h'(\eta)]$, temperature profile and concentration profile will be obtained for numerous values of Deborah number β, the mixed convection parameter Ri, the Soret number Sr, Dufour number Db, Schmidt number Sc and Prandtl number Pr. This numerical technique contains Code A, and it is executed to acquire the solutions numerically for any values of autonomous variables. Hence, the ruling equations [Eqs. (8) - (11)] with the boundary conditions [Eq. (12)] are applied in the MATLAB bvp4c coding. Finally, the following variables are introduced:

$$y(1)=f,y(2)=f',y(3)=f'',y(4)=f''',y(5)=h,$$
$$y(6)=h',y(7)=\theta,y(8)=\theta',y(9)=\phi,y(10)=\phi'. \tag{15}$$

By using these variables, Eqs. (8) - (11) are converted to,

$$\left(\frac{8}{B\eta(y(2)+y(6))}\right)\begin{pmatrix}2y(2)[y(2)+y(6)]-y(3)[y(1)+y(5)]-\frac{1}{\eta^2}[y(2)+\eta y(3)]-y(4)\\-[y(2)+y(6)]\left[\frac{3}{4}By(4)+\frac{B}{\eta^2}y(2)\right]+\frac{3B}{2\eta}y(3)\\-(1+L)\left\{Ri[y(7)+Ny(9)]-\frac{M}{\eta^2}y(2)\right\}\end{pmatrix}, \tag{16}$$

$$2y(6)[y(2)+y(6)]-\frac{1}{\eta^2}[y(2)+\eta y(3)]-y(4)-\frac{B\eta}{8}y(5)[y(2)+y(6)]-[y(2)+y(6)]$$
$$\left(\left[\frac{3}{4}By(4)+\frac{B}{\eta^2}y(2)\right]+\frac{3B}{2\eta}y(3)-(1+L)\left\{Ri[y(7)+Ny(9)]-\frac{M}{\eta^2}y(2)\right\}\right), \tag{17}$$

$$\left(\frac{Pr}{(1-Db)ScSrPr}\right)([y(2)+y(6)][y(7)-DbScy(9)]+[y(1)+y(5)]\{DbSc[y(10)-y(8)]\}), \tag{18}$$

$$\left(\frac{Sc}{(1-Db)ScSrPr}\right)([y(9)-PrSry(7)][y(2)+y(6)]-[y(1)+y(5)][y(10)-PrSry(8)]). \tag{19}$$

Similarly, Eq. (12) is transformed as given below:

$$ya(1)=I,ya(2)=\mu_1,ya(5)=0,ya(6)=\mu_2,ya(7)=1,ya(9)=1,$$
$$yb(2)\to 0,ya(6)\to 0,ya(7)\to 0,ya(9)\to 0, \tag{20}$$

where ya and yb refers to the boundary conditions on the wall and away from the wall respectively. Eqs. (16) - (19) together with Eq. (20) are used to develop the MATLAB coding using the bvp4c solver function.

2.2 Comparison with Previous Results

To test the precision of the applied numerical method, the current findings are rationalised by collating with previous data. Accordingly, the current findings are collated with the numerical findings reported by Parvin et al. [26, 27]. The comparison for the gradient of temperature on the wall, $\theta'(0)$ among the current findings and the previous findings are shown in Table 1. As a conclusion, the present values of the solution for $\theta'(0)$ are in great resemblance with those reported by preceding researchers. Thus, the fine comparison provides us sufficient credence and confidence to conduct our study both theoretically and numerically.

Table 1. Similarity of the temperature gradient values on the wall, $\theta'(0)$ for numerous values of Pr when $M = N = Ri = Sc = Sr = Db = B = I = 0$

μ	Pr	Parvin et al. [27]	Parvin et al. [26]	Present
	1			-1.04591
1.2	3	-	-	-2.04747
	5			-2.73876
	1		-1.00139	-1.00139
1.1	3	-	-1.96030	-1.96030
	5		-2.62216	-2.62216
	1	-0.95478	-0.95478	-0.95478
1	3	-1.86907	-1.86907	-1.86907
	5	-2.50013	-2.50013	-2.50013
	1	0.90579	0.90579	0.90579
0.9	3	1.77316	1.77316	1.77316
	5	0.07692	0.07692	0.07692

3. Results and Discussion

Figures 2-4 show the components of velocity along the x and y-axes subject to the influence of $|I|$, Ri, and N respectively. Based on the injection parameter, the values are supposed to be negative values (-0.1, -0.3, -0.5) but the injection rate changes to the positive values with the presence of $|I|$ to show the increment of I easily. Overall, it could be noticeable from Figure 2(a) such that the fluid's velocity continously increases with the increment in $|I|$ for horizontal component. The velocity for the vertical component (Figure 2 (b)) is seen to increase and decrease with the increment of I as the maximum peak occurs for the lowest value $|I| = 0.1$, then it increases with the increment of $|I|$ and $\eta \geq 1.5$. The velocity turns up from the maximum peak eventually reaching the ambient velocity approximately. This behaviour contributes to the broadening of the boundary layer for both velocity components as greater injection is applied to the flow. Increasing the injection parameter creates drag, which in turn elevates the magnitude of the velocity.

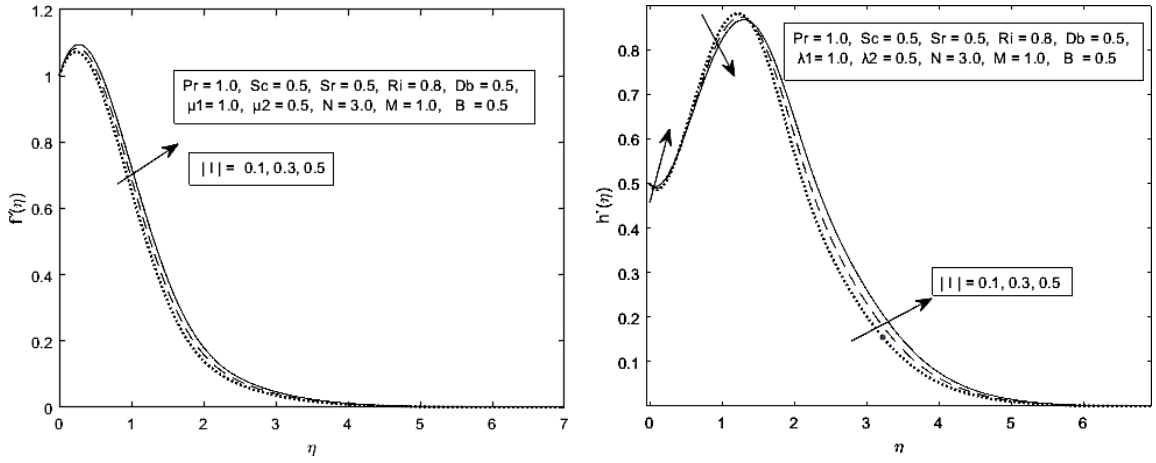

(a) (b)

Figure 2. Velocity profiles for (a) the horizontal axis $f'(\eta)$ and (b) vertical axis $h'(\eta)$ for diverse values of the injection parameter $|I|$

The outturn of the mixed convection parameter Ri on the velocity is pictured in Figure 3. A maximum peak of velocity happens nearer the sheet (small η) when greater Ri is imposed. Increment in Ri increases the velocity for thinner boundary layer whilst gives reverse impact when the boundary layer gets thicker. The dissimilarity of the magnitude for both components of the velocity is observable closer to the sheet. However, it becomes insignificant for greater η. Graphically, it could be noticed from Figure 3 that the maximum peak for both components occurs for the biggest Ri value for assisting stream. However, the peak of horizontal component is greater than vertical component. In addition, as the boundary layer becomes thicker, the velocity gradually approaches zero, indicating that the fluid stabilizes and becomes motionless far from the surface. The fluid's velocity inclines and decreases in certain range as the mixed convection parameter is augmented for both cases. But Figure 3(b) is seen to decrease and increase with the increment of I as the maximum peak happens at the greatest value $Ri = 1.2$, then it decreases with the increment of Ri and $\eta \geq 2.5$. The velocity turns down from the maximum peak until it reaches approximately the ambient velocity.

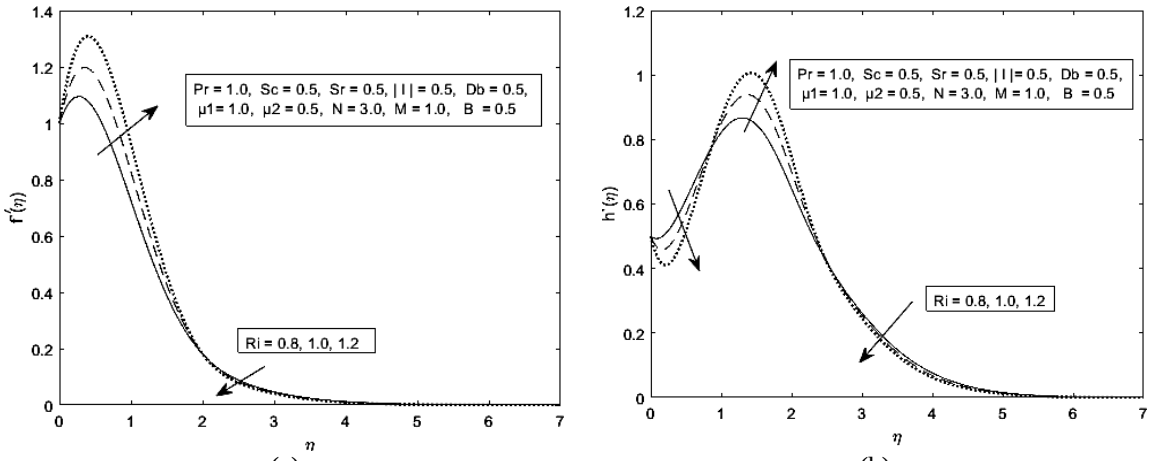

(a) (b)

Figure 3. Velocity profiles for (a) the horizontal component $f'(\eta)$ and (b) vertical component $h'(\eta)$ for diverse values of the mixed convection parameter Ri

The influence of the buoyancy ratio N on the velocity profile is delineated in Figure 4. In the attendance of a bigger N, highest peak appears nearby to the plate (small η). For thin boundary layer, augmentation in N values incline the velocity, and a contrary trend is spotted for a broader η. From this graph, a maximum peak of both components appears for the biggest N nearby to extending sheet for the assisting flow. Despite this, the horizontal component possesses bigger maximum value compared to vertical component. After the maximum peak for Figure 4(a), the maximum point $N = 3.4$ happens for opposing stream. Additionally, the fluid reaches a stable state as the boundary layer thickness inclines. The fluid's velocity elevates and decreases in certain range as the buoyancy parameter is increased for both cases. But Figure 4(b) is seen to decrease and increase with the increment of I as the maximum peak exists for the biggest value $N = 3.4$, then it decreases with the increment of N and $\eta \geq 2.5$. The velocity turns down from the maximum peak until it reaches approximately the ambient velocity.

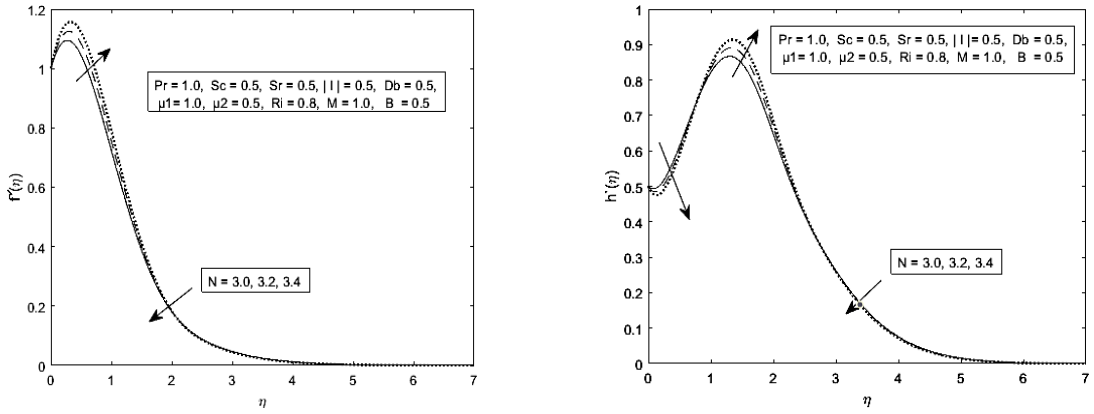

(a) (b)

Figure 4. Velocity profiles for (a) the horizontal axis $f'(\eta)$ and (b) vertical axis $h'(\eta)$ for diverse values of the buoyancy parameter N

An opposite analysis was made for the temperature profile in Figure 5. The temperature profile $\theta(\eta)$ for different values of Sr and Db are illustrated respectively in this figure. Figure 5(a) illustrates that the temperature decreases continuously for all values of η. As Sr increases, it is noticed that the temperature deteriorates near to the sheet but varies oppositely when $\eta \geq 1.5$ approximately. It is also perceptible from Figure 5(b) that the inclination of temperature is pivotal closer the sheet and converts moderately to the peripheral temperature for higher η. An increase in temperature difference enhances thermal energy movement from the cooler to the hotter region, which is attributed to the Dufour effect. Accordingly, Figure 5(b) outlines that the boundary layer broadness and temperature are intensified with the surging of Db. Therefore, the temperature increases due to the increment of the Dufour effect and for the Soret effect, it decreases and increases with the increment of Sr. The Dufour effect refers to the phenomenon where temperature gradients induce mass exchange within a fluid. In the context of double diffusive flows, the Dufour effect can influence the temperature profile by causing variations in mass transport rates. Higher temperature gradients can lead to enhanced mass transfer, affecting the concentration profile in the fluid. This effect is often described by the Dufour coefficient, which exhibits the thermal exchange and mass exchange ratio.

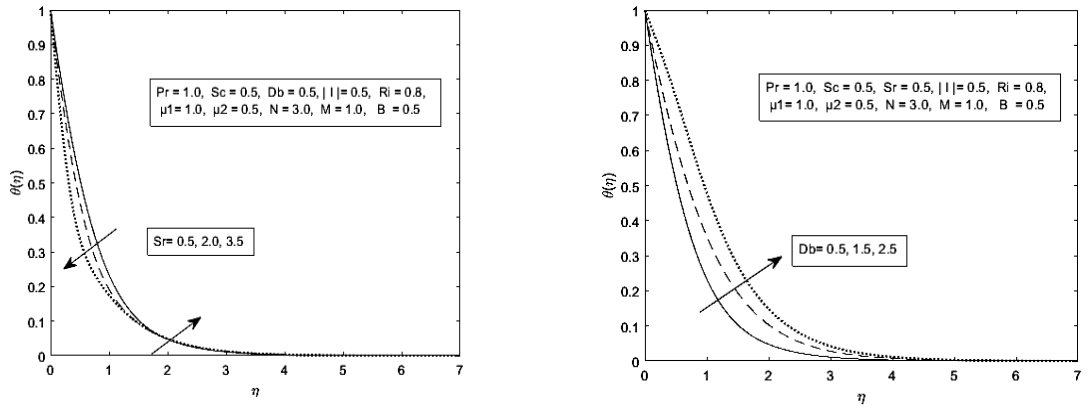

(a) (b)

Figure 5. Temperature profile $\theta(\eta)$ for diverse values of (a) the Soret number Sr and (b) Dufour number Du

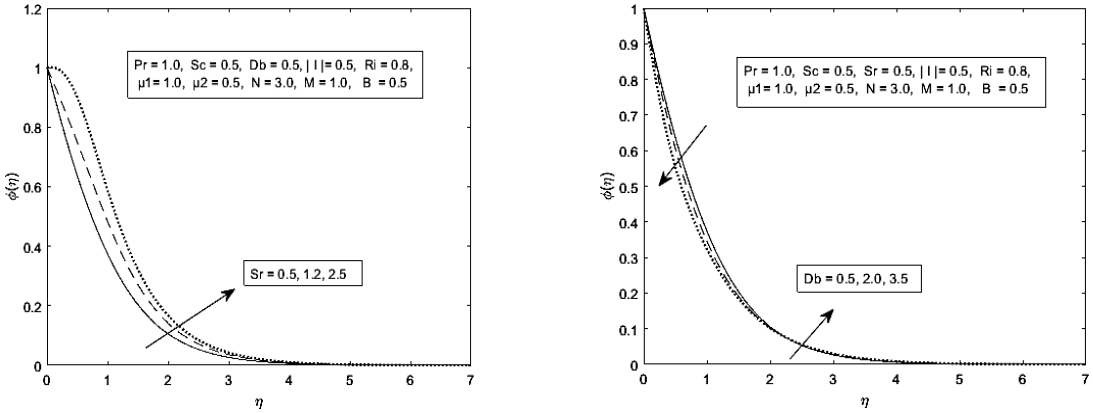

(a) (b)

Figure 6. Concentration profile $\phi(\eta)$ for diverse values of (a) the Soret number Sr and (b) Dufour number Du

The concentration's profiles for non-similar values of Sr and Db, respectively, are portrayed in Figure 6. The exchange of mass from smaller to greater concentration region due to the temperature difference is determined by the Soret effect. Figure 6(a) exhibits the continual increment of the concentration for all ranges of η. It is noticeable that the elevation of concentration is notable near the sheet and gradually becomes normal temperature for greater η. Besides, Figure 6(b) depicts the temperature decreasing as the value of Db is increased near the sheet and it acts reversely when $\eta \geq 2.0$. Thus, the concentration increases because of inclining Soret number (Figure 6(a)). In Figure 6(b), the concentration profile deteriorates and rises with the increment of Db. The Soret effect is related to the consequences of concentration gradients on heat dispersal within a fluid. In the existence of concentration gradients, the Soret effect can lead to variations in temperature, influencing the thermal profile of the fluid. In double diffusive flows, the Soret effect becomes crucial as it introduces a coupling between temperature and concentration fields, affecting both heat and mass transport.

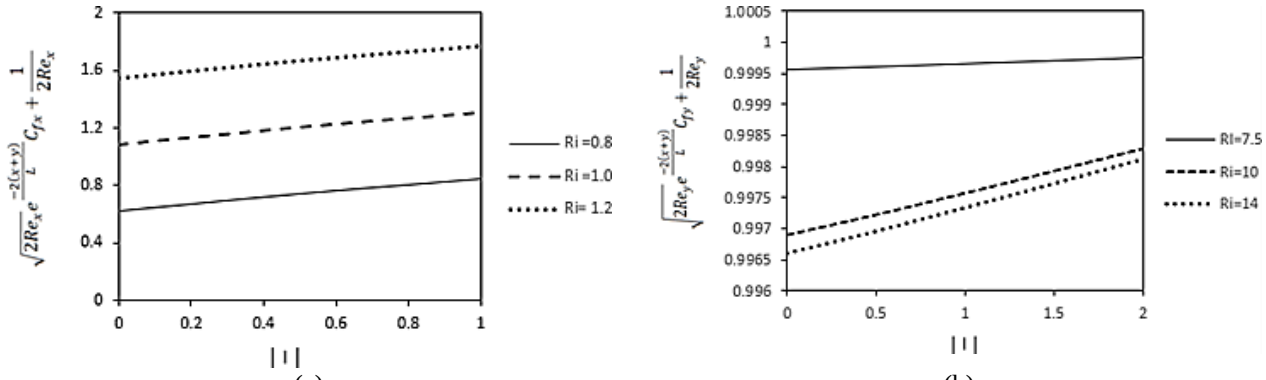

(a) (b)

Figure 7. Skin friction coefficient in (a) the horizontal component $\sqrt{Re_x}e^{-\frac{(x+y)}{L}}C_{fx}+\frac{1}{2Re_x}$ and (b) the vertical component $\sqrt{Re_y}e^{-\frac{(x+y)}{L}}C_{fy}+\frac{1}{2Re_y}$ versus injection parameter $|I|$ for diverse values of the mixed convection parameter Ri

Figure 7 and Figure 8 showcase the skin friction coefficient along x and y-axes, respectively. Precisely, the effects of $|I|$ and Ri on the skin friction coefficient is delineated in Figure 7. The value of the skin friction coefficient increases as

a response to the uplift of Ri in horizontal direction while it decreases for vertical direction. The influence of the mixed convection parameter does not yield a notable variation in the vertical components of skin friction coefficient. However, the horizontal component possesses a perceivable change for the same parameter. For all ranges of $|I|$, the skin friction coefficients drop down. Concurrently, the effect of $|I|$ and N on the skin friction coefficient is resented in Figure 8. The dissimilarity of the skin friction coefficient for horizontal component inclines with the growth of N , for the increment of injection rate parameter $|I|$ (assisting stream) while it decreases for vertical component. It is worth mentioning that the flow accelerates in the case of assisting flow as N increases. Consequently, the local skin friction coefficient for horizontal component expands in Figure 8(a). Figure 8(b) portrays that the stream of fluid decelerates since the local skin friction coefficient decreases and reaches approximately the ambient velocity.

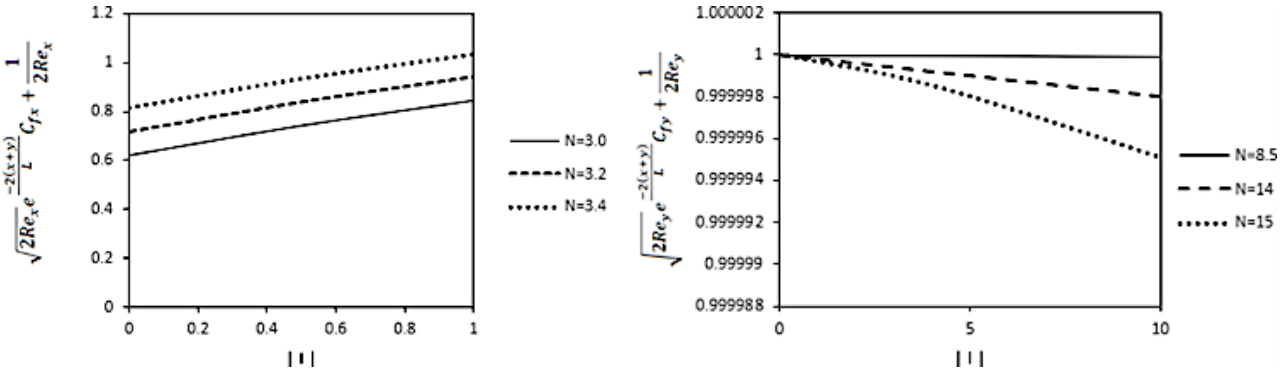

(a) (b)

Figure 8. Skin friction coefficient in (a) the horizontal component $\sqrt{Re_x}e^{-\frac{(x+y)}{L}}C_{fx}+\frac{1}{2Re_x}$ and (b) the vertical component $\sqrt{Re_y}e^{-\frac{(x+y)}{L}}C_{fy}+\frac{1}{2Re_y}$ versus injection parameter $|I|$ for diverse values of the buoyancy parameter N

The local Nusselt number $Nu_x\sqrt{\frac{2}{Re_x}}$ against $|I|$ for different values of Sr is presented in Figure 9(a). Whilst $Nu_x\sqrt{\frac{2}{Re_x}}$ against $|I|$ for diverse values of Db is displayed in Figure 9(b). Additionally, the local Sherwood number $Sh_x\sqrt{\frac{2}{Re_x}}$ against $|I|$ for non-similar values of Sr and Db are showcased in Figure 10(a) and Figure 10(b) respectively. The values of $Nu_x\sqrt{\frac{2}{Re_x}}$ grows when both the injection rate parameter $|I|$ and the Soret effect Sr are intensified (Figure 9(a)). A similar trend is discerned for the local Sherwood numbers affected by both $|I|$ and the Dufour effect Db (Figure 10(b)). The local Nusselt number (Figure 9(a)) alongside the local Sherwood number (Figure 10(b)) increase for the increment of $|I|$. In Figure 9(b), it is perceivable that the local Nusselt number decreases with the augmentation of Db and the same profile pattern is observed in Figure 10(a). Based on Figure 9, it shows that the Soret number positively affects the Nusselt number. It shows the same in Figure 10 as Dufour number Db positively influence the Sherwood number.

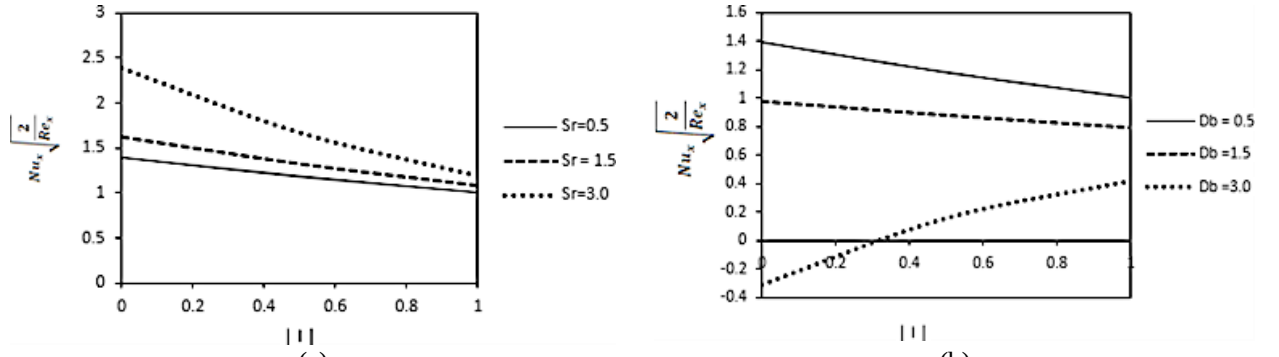

(a) (b)

Figure 9. Local Nusselt number $Nu_x\sqrt{\frac{2}{Re_x}}$ versus injection effect parameter $|I|$ (a) for diverse values of the Soret number Sr and (b) for diverse values of the Dufour number Db

The Nusselt number characterizes the convective heat exchange and conductive heat exchange ratio along a boundary layer. For a fluid system influenced by the Dufour effect, an uplift in the Dufour number Db signifies enhanced thermal diffusion effects. This can lead to change in temperature gradients and, consequently, impact the Nusselt number. The relationship between Dufour number and Nusselt number rely on the attributes of the fluid flow and boundary conditions. Besides, the Sherwood number marks the proportion of convective mass exchange to diffusive mass exchange along a

boundary layer. For a fluid system influenced by the Soret effect, an uplift in the Soret number Sr indicates enhanced thermo-diffusion effects, leading to change in concentration gradients and affecting the Sherwood number.

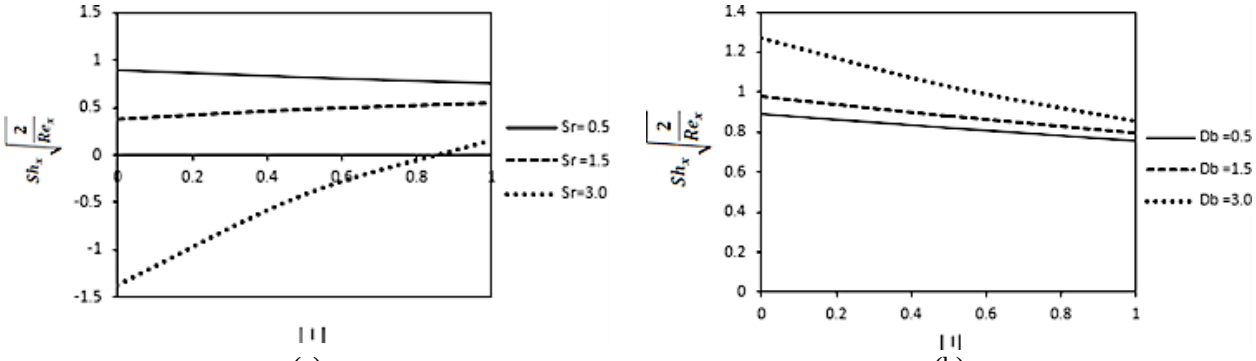

(a) (b)

Figure 10. Local Nusselt number $Sh_x\sqrt{\frac{2}{Re_x}}$ versus injection effect parameter $|I|$ (a) for diverse values of the Soret number Sr and (b) for diverse values of the Dufour number Db

4. Conclusions

The grail of current study is to construct a mathematical framework for thermal properties of Jeffrey fluid flow with injection effect over an extending sheet. The model comprises of continuity equation, momentum equations in ($x-$, $y-$axes), thermal equation, concentration equation, and the boundary constraints. The equations which in the structure of partial differential equations are altered into ordinary differential equations by applying similarity transformation. The suitable boundary conditions for the ordinary differential equations are also found using the similar step. The equations are then executed in bvp4c solver rendered by MATLAB software to curb the numerical findings. The resulting findings are velocity profiles for x and y components, temperature, and concentration. Later, the effects of the mixed convection parameter Ri, the bouyancy ratio N , the injection rate $|I|$, the Soret number Sr and Dufour number Db parameters on the developed model are probed by altering the values of respective parameters within the coding and noticing the trends of the solutions for each profile. The graphical presentation of these behaviours is presented.

The velocity of the flow shoots up as the injection rate parameter increased for a larger η. The stream velocity also inclines with the escalation of the mixed convection parameter Ri and the buoyancy parameter N for a minor broadness of the boundary layer, and it behaves in reverse manner distant from the sheet. Temperature profile increases for several values of Db and the concentration profiles upsurges for numerous values of Sr. It proves that the temperature is affected by Db and concentration profile is influenced by Sr. The skin friction coefficient for horizontal direction uplifts with the escalation of I in numerous values of Ri and N . The skin friction coefficient for vertical direction decreases with the augmentation of I in diverse values of Ri and N . The local Nusselt number elevates with the escalation of Sr and the local Sherwood number uplifts with the increasing of Db. The Soret effect can influence the Nusselt number in the context of thermal exchange and in the context of mass exchange, the Dufour impact can influence the Sherwood number.

Acknowledgement

The authors gratefully acknowledge the Universiti Putra Malaysia for supporting this work.

Funding

This study was supported by a grant from Universiti Putra Malaysia (Project code: GPI / 2023 / 9766100).

Declaration of Competing Interest

The authors declare no conflict of interest.

CRediT Authorship Contribution Statement

Nanthini Balakrishnan (Validation; Writing - review & editing)
Fatin Nur Asyikyn Pazil (Formal analysis; Investigation; Writing - original draft)
Shahanaz Parvin (Methodology; Visualisation)
Nurul Syuhada Ismail (Conceptualisation; Writing - review & editing)
Siti Suzilliana Putri Mohamed Isa (Funding acquisition; Project administration; Supervision)

Availability of the Data and Materials

The data used to support the findings of this study are included within the article.

Ethical Declaration

No artificial intelligence tools were used in the preparation of this manuscript. All content was developed manually by the authors. This study did not involve human participants or animals. Ethical approval was therefore not required.

Generative Artificial Intelligence Declarations

The authors claim that artificially intelligent-assisted technologies in the form of generative AI were not used to generate content, ideas, or theories. We have just utilised AI to enhance readability and refine the language. This was used with extreme human control and oversight. The authors take full responsibility for reviewing and approving the content.

References

[1] Elsaid EM. Simulation of blood flow in a tapered artery with ternary hybrid nanofluid and Jeffrey model. Modern Physics Letters B. 2025 Jul 20;39(20):2550056.
[2] Raikher YL, Rusakov VV, Perzynski R. Brownian motion in a viscoelastic medium modelled by a Jeffreys fluid. Soft Matter. 2013;9(45):10857-10865.
[3] Ge-JiLe H, Nazeer M, Hussain F, Khan MI, Saleem A, Siddique I. Two-phase flow of MHD Jeffrey fluid with the suspension of tiny metallic particles incorporated with viscous dissipation and porous medium. Advances in Mechanical Engineering. 2021 Mar;13(3):16878140211005960.
[4] Morris JF. Toward a fluid mechanics of suspensions. Physical Review Fluids. 2020 Nov;5(11):110519.
[5] Khan A, Gul T, Ali I, Khalifa HA, Muhammad T, et al. Thermal examination for double diffusive MHD Jeffrey fluid flow through the space of disc and cone apparatus subject to impact of multiple rotations. International Journal of Heat and Fluid Flow. 2024 Apr 1;106:109295.
[6] Ajithkumar M, Lakshminarayana P. Chemically reactive MHD peristaltic flow of Jeffrey nanofluid via a vertical porous conduit with complaint walls under the effects of bioconvection and double diffusion. International Journal of Modern Physics B. 2024 Jun 30;38(16):2450203.
[7] Alqudah M, Imran A, Assiri TA, Alshehri NA, Alfwzan WF, et al. Investigation of thermal radiations impacts with double diffusive convection for Prandtl nanofluid with slip in an asymmetric ciliated channel. Case Studies in Thermal Engineering. 2024 May 1;57:104305.
[8] Kanimozhi N, Vijayaragavan R, Rushi Kumar B, Chamkha AJ. Investigation of Hall current and thermal diffusion effects on unsteady MHD mixed convective Jeffrey fluid flow over an inclined permeable surface with chemical reaction. The European Physical Journal Plus. 2024 Mar;139(3):1-6.
[9] Parvin S, Balakrishnan N, Isa SS. MHD Casson fluid flow under temperature and concentration gradients. Magnetohydrodynamics. 2021 Jul 1;57(3): 353-366.
[10] Sahoo A, Nandkeolyar R. Radiative heat transport of Cattaneo-Christov double diffusive Casson nanofluid flow between two rotating disks with Hall current and activation energy. ZAMM-Journal of Applied Mathematics and Mechanics. 2024 Feb;104(2):e202200419.
[11] Paandurangan B, Errappa Parthasarathy S, Tripathi D, Bég OA. The impact of double-diffusive convection on electroosmotic peristaltic transport of magnetized Casson nanofluid in a porous asymmetric channel. ZAMM-Journal of Applied Mathematics and Mechanics. 2024 Sep;104(9):e202300771.
[12] Parvin S, Isa SS, Jamshed W, Ibrahim RW, Nisar KS. Numerical treatment of 2D-Magneto double-diffusive convection flow of a Maxwell nanofluid: heat transport case study. Case Studies in Thermal Engineering. 2021 Dec 1;28:101383.
[13] Khan MN, Wang Z, Ahammad NA, Rezapour S, Shutaywi M, et al. Mixed convective flow analysis of a Maxwell fluid with double diffusion theory on a vertically exponentially stretching surface. Applied Water Science. 2024 Aug;14(8):172.
[14] Upreti H, Bisht A, Joshi N. MHD Darcy–Forchheimer flow and double-diffusive modeling of Maxwell fluid over rotating stretchable surface: a computational study. Modern Physics Letters B. 2024 Sep 30;38(27):2450227.
[15] Hamza M. Double-diffusive convection in flow of Carreau fluid with variable density inside converging and diverging channels of rectilinear walls. Results in Engineering. 2024 Dec 1;24:103053.
[16] Padma SV, Mallesh MP, Jamuna B, Reddy SR, Jakeer S. Exploring double-diffusive convection in ferromagnetic Carreau nanofluid with magnetic dipole: insights for solar thermal systems over plate, wedge, and stagnation. Case Studies in Thermal Engineering. 2024 Sep 1;61:104952.
[17] Alomari MA, Al-Farhany K, Al-Salami QH, Alyousuf FQ, Ali IR, et al. Numerical analysis of double-diffusive free convection in a curvilinear cavity filled with nanofluid and triple fins attached to the hot walls. The European Physical Journal Plus. 2024 Feb 9;139(2):149.
[18] Prajapati VJ, Meher R. Analysing Soret, Dufour, and activation energy effects on heat and mass transfer thin film flow of an MHD Williamson ternary hybrid nanofluid over a non-Darcy porous stretching surface. The European Physical Journal Plus. 2025 Mar 1;140(2):177.
[19] Mng'ang'a J, Richard Onyango E. Joule heating and induced magnetic field on magnetohydrodynamic generalised Couette flow of Jeffrey fluid in an inclined channel with Soret and Dufour effects. International Journal of Ambient Energy. 2024 Dec 31;45(1):2305328.

[20] Mahla R, Kaladhar K. Effect of Hall current, Soret number, and inclined magnetic field on entropy generation of mixed convection Jeffrey fluid flow through sloping channel under Navier-slip condition. ZAMM-Journal of Applied Mathematics and Mechanics. 2024 Apr;104(4):e202300700.
[21] Ullah H, Alqahtani AM, Raja MA, Fiza M, Ullah K, et al. Numerical treatment based on artificial neural network to Soret and Dufour effects on MHD squeezing flow of Jeffrey fluid in horizontal channel with thermal radiation. International Journal of Thermofluids. 2024 Aug 1;23:100725.
[22] Basha H. Heat and mass transport phenomenon on 3D MHD Jeffery nano-liquid past an exponentially stretchable sheet subject to Soret and Dufour effect: optimal solutions. ZAMM-Journal of Applied Mathematics and Mechanics. 2024 Apr;104(4):e202300602.
[23] Fard MS, Torabiyan A, Jalili P, Jalili B, Ganji DD. Investigating the magnetohydrodynamics non-Newtonian fluid movement on a tensile plate affected by variable thickness with Dufour and Soret effects: Akbari Ganji and finite element methods. International Journal of Electrochemical Science. 2024 Aug 1;19(8):100701.
[24] Sudarmozhi K, Iranian D, Khan I, Hajjej F, Omer AS, et al. Heat generation in dual convection non-Newtonian MHD Darcy's flow with Soret and Dufour effects. Case Studies in Thermal Engineering. 2024 Jan 1;53:103704.
[25] Parvin S, Isa SS, Soid SK. Three-dimensional model of double diffusive magnetohydrodynamic Newtonian fluid flow. Magnetohydrodynamics. 2021 Jul 1;57(3):365-376.
[26] Ahmad K, Hanouf Z, Ishak A. Mixed convection Jeffrey fluid flow over an exponentially stretching sheet with magnetohydrodynamic effect. AIP Advances. 2016 Mar 1;6(3):035012.
[27] Parvin S, Isa SS, Arifin NM, Ali FM. Soret and Dufour effects on magneto-hydrodynamics Newtonian fluid flow beyond a stretching/shrinking sheet. CFD Letters. 2020;12(8):85-97.